Mott metal-insulator transitions in pressurized layered trichalcogenides

Heung-Sik Kim,[1] Kristjan Haule,[1] and David Vanderbilt[1]

[1]*Department of Physics and Astronomy, Rutgers University, Piscataway, New Jersey 08854-8019, USA*

Transition metal phosphorous trichalcogenides, MPX_3 (M and X being transition metal and chalcogen elements respectively), have been the focus of substantial interest recently because of their possible magnetism in the two-dimensional limit. Here we investigate material properties of the compounds with M = Mn and Ni employing *ab-initio* density functional and dynamical mean-field calculations, especially their electronic behavior under external pressure in the paramagnetic phase. Mott metal-insulator transitions (MIT) are found to be a common feature for both compounds, but their lattice structures show drastically different behaviors depending on the relevant orbital degrees of freedom, *i.e.* t_{2g} or e_g. $MnPS_3$ undergoes an isosymmetric structural transition by forming Mn-Mn dimers due to the strong direct overlap between the neighboring t_{2g} orbitals, accompanied by a significant volume collapse and a spin-state transition. In contrast, $NiPS_3$ and $NiPSe_3$, with their active e_g orbital degrees of freedom, do not show a structural change at the MIT pressure or deep in the metallic phase. Hence $NiPS_3$ and $NiPSe_3$ become rare examples of materials hosting electronic bandwidth-controlled Mott MITs, thus showing promise for ultrafast resistivity switching behavior.

Although the Mott transition was first identified by Mott and Peierls in 1937 [1], and the canonical model for the metal-insulator transition was proposed by Hubbard in 1963 [2], there are very few solids that are known to undergo purely electronic and bandwidth-controlled metal-insulator transitions (MITs), as was originally envisioned by Hubbard. By a purely electronic transition we mean one that does not involve a strong structural distortion or a concomitant structural phase transition. Even less common are such transitions in two-dimensional materials, and to our knowledge there is no known example of an electronically driven MIT among the van der Waals (vdW) materials.

Electronic bandwidth-controlled MITs can be very useful for practical applications because the switching can be extremely fast, as it does not involve the slow lattice degrees of freedom. Moreover, the induced metallic state has better mobility because of the reduced density of impurities compared to doped Mott insulators. The fast switching in the two-dimensional vdW materials might be useful for ultrathin electronic and spintronic applications.

The most commonly studied examples of MITs are either *a*) the filling-controlled one, such as the doped cuprates [3], or *b*) the MIT strongly coupled with the lattice degrees of freedom, such as in the rare-earth nickelates $R\mathrm{NiO_3}$ (R being a rare-earth element) [4, 5]. The filling-controlled MIT of type (*a*) inevitably leads to strong inhomogeneity at the atomic scale due to the impurities introduced by the chemical doping. Hence, it is difficult to access the homogeneous limit, and electronic mean free path tends to be exceptionally short because the correlation strength in such systems is typically far above the critical value [6]. Among the systems that undergo bandwidth-induced MITs of type (*b*), the most often studied materials include V_2O_3 [7–9], VO_2 [7, 10], and $R\mathrm{NiO_3}$ [4, 5]. In all these examples, the structural degrees of freedom play a crucial role at the transition.

From the theoretical side, there is growing evidence that starting from the metallic side, the MIT would not have occurred in any of these three systems in the absence of a simultaneous structural distortion. For example, the bond disproportionation between the short and long Ni-O bonds is crucial for the appearance of the Mott state in $R\mathrm{NiO_3}$ [11–14]. Similarly, the dimerization of vanadium atoms is crucial for the occurrence of the insulating state in monoclinic VO_2 [15, 16]. Interestingly, there have been several recent reports that the MIT in VO_2 can be decoupled from the monoclinic-to-rutile structural transition [17, 18], and there is supporting experimental evidence of the existence of a monoclinic metallic state [19]. Because of this decoupling of the electronic and lattice transitions, the MIT and the resistive switching in VO_2 can be record-fast [20, 21].

Here we propose new candidates for the electronic bandwidth-controlled MIT without significant structural distortion among the emerging class of two-dimensional vdW materials. Our target is a series of transition metal phosphorous trichalcogenides MPX_3 (M = Mn, Ni, X = S, Se) [23]. To incorporate the electronic and structural degrees of freedom on an equal footing, we employ the state-of-the-art embedded dynamical mean-field theory combined with density functional theory (eDMFT), which implements forces on atoms and allows relaxation of internal atomic coordinates [24]. For the optimization of the size and shape of unit cells we use density functional theory (DFT) augmented by the on-site Coulomb repulsion U (DFT+U), after which optimizations of internal atomic coordinates are performed both in eDMFT and DFT+U yielding consistent results[25]. We mainly focus on paramagnetic phases of $MnPS_3$ and $NiP\{S,Se\}_3$ above their Néel temperatures (T_N = 78 and 154 K for $MnPS_3$ and $NiPS_3$ respectively [26–28]), with disordered local Mn^{2+} (d^5) $S = 5/2$ and Ni^{2+} (d^8) $S = 1$ moments, although the behavior of their MITs in the magnetic phases is discussed in the Supplementary Information (SI). We will show that the recently discovered MIT in $MnPS_3$ [22] falls under the family of transitions coupled to structural changes, in which the dimerization plays a crucial role, therefore bearing a resemblance to the MIT in VO_2. On the other hand, theoretical simulations in $NiPS_3$ and $NiPSe_3$ suggest that the MIT in these two vdW compounds occurs at even lower pressure, and does not involve a simultaneous

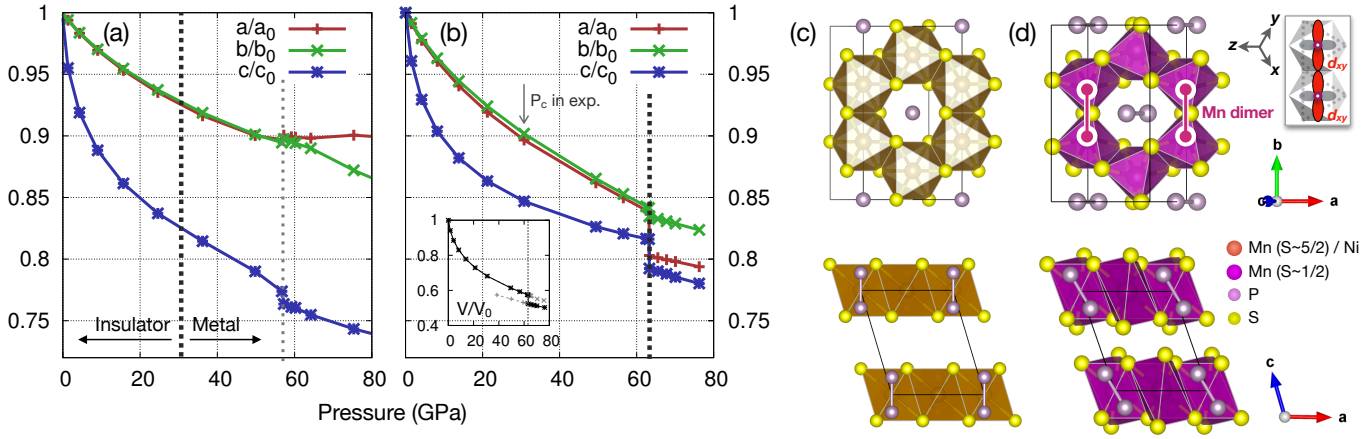

FIG. 1. (a,b) Evolution of lattice parameters (a, b, and c as depicted in (d)) of (a) $NiPS_3$ and (b) $MnPS_3$ from DFT+U calculations as a function of pressure. Inset in (b) shows a volume versus pressure plot for $MnPS_3$. Thick vertical dashed lines in both plots indicate the values of critical pressure where the MIT happens. The thin dotted line in (a) shows the pressure where the a/a_0 and b/b_0 begin to branch in $NiPS_3$ (*i.e.* $b \neq \sqrt{3}a$) due to the enhanced monoclinicity by pressure. Note that, the critical pressure for $MnPS_3$ reported in Ref. 22 is around 30 GPa, as depicted in the figure. (c) Crystal structures for $NiPS_3$ and $MnPS_3$ at the ambient pressure. (d) $MnPS_3$ structure when P $>$ 64 GPa, where the Mn-dimer is formed parallel to b.

structural transition. Therefore they become rare examples of electronic bandwidth-controlled transitions with a potential for very fast resistive switching.

Crystal structures versus pressure. Fig. 1(a) and (b) show DFT+U results on the pressure-induced change of the three lattice parameters (a/a_0, b/b_0, and c/c_0, where $\{a, b, c\}_0$ denote their zero-pressure values) for $NiPS_3$ and $MnPS_3$, respectively. Because both of the compounds are vdW-type layered systems, the inter-plane lattice parameter c shows a steeper decrease compared to the in-plane a and b, and the three-fold symmetry within each layer forces $b \simeq \sqrt{3}a$ in the low-P regime. The resulting volume decrease under pressure is substantial: 40% of volume reduction at $\sim$ 50 GPa compared to the ambient pressure volume, as shown in the inset of Fig. 1(b).

Both compounds show MIT and structural phase transitions under pressure, but the nature of their transition is drastically different. As shown in Fig. 1(a), the MIT and the structural transition in $NiPS_3$ occur at very different pressures, around 31 and 57 GPa respectively, while they coincide in $MnPS_3$. Remarkably, theoretical simulations suggest that the MIT in $NiPS_3$ accompanies no significant structural distortion (discontinuous structural changes, for example), and is thus a rare example of an electronically driven bandwidth-controlled MIT. On the other hand, in $MnPS_3$ the isosymmetric structural transition (*i.e.*, structural transition within the same space group symmetry) with a volume collapse at 63 GPa is crucial for the occurrence of the MIT, hence the transition is better classified as the structurally assisted MIT (see Fig. 1(b)). We note that the theoretical critical pressure of 63 GPa is somewhat overestimated compared to the experimentally reported value of $\sim$ 30 GPa [22]. However, we show in the SI that within eDMFT, spinodal lines extend down to a much lower pressure of 40 GPa with a much reduced energy barrier between the metallic and insulating solutions compared to the DFT+U results. Inclusion of the phonon free energy and the lattice zero-point energy, which is neglected here, could then move the position of the transition significantly (see the SI for further details).

In addition to the volume collapse, mostly from the discontinuous change of a, DFT+U simulations of $MnPS_3$ show a Mn-Mn dimerization along the b-direction with the tilting of the P_2 dimer as shown in Fig. 1(d). The Mn-Mn bond lengths between the dimer and non-dimer bonds are 2.42 and 3.10 Å at 63 GPa, respectively, which is a rather large difference. This Mn dimer formation is attributed to the direct d-d overlap between the Mn t_{2g} orbitals, pointing directly towards the nearest-neighbor Mn as shown in the inset of Fig. 1(d). Note that the previous experimental study suggested the formation of Mn zigzag chains in the high-P phase [22], in contrast to our DFT+U and eDMFT results.

$NiPS_3$, on the other hand, shows no such intermetallic dimerization or chain formation at the MIT or beyond the structural transition pressure, because the partially-filled Ni e_g orbitals point towards the S atoms. This makes $NiPS_3$ more sensitive to the p-d hybridization, yielding a smaller MIT pressure in $NiPS_3$ compared to $MnPS_3$. Such a stark contrast between $NiPS_3$ and $MnPS_3$, originating from the difference in their orbital physics, affects the nature of the structural behavior of their MIT as shown below. Note that the structural transition in $NiPS_3$ at 57 GPa is not orbital in nature and comes purely from the reduced interlayer distance and the large overlap between the layers.

We note that the two compounds show markedly different pressure dependence of the lattice parameters even before the structural transition. By comparing Fig. 1(a) and (b) it is evident that the compression of c under pressure is stronger in $NiPS_3$ than in $MnPS_3$; while $a/a_0 - c/c_0$ in $MnPS_3$ at 60

GPa is about 0.03 (See Fig. 1(b)), in $NiPS_3$ it is about 0.15 (Fig. 1(a)) despite the similar volume change. In other words, it is much easier to compress $NiPS_3$ along the layer-normal direction compared to $MnPS_3$. Because the kinetic energy scale set by the hopping integrals between the t_{2g} (for $MnPS_3$) and e_g (for $NiPS_3$) orbitals show different anisotropy, the t_{2g} and e_g yield strong in-plane d-d and inter-plane d-p-p-d overlaps respectively (See SI). As a result, while the t_{2g} orbitals favor in-plane compression for the larger in-plane kinetic energy gain, the e_g orbitals prefer to reduce the inter-plane distance, yielding the tendency shown in Fig. 1(a) and (b).

Electronic MIT in $NiPS_3$. Below we take a closer look into the nature of the MIT in $NiPS_3$. Note that all the spectra presented hereafter are eDMFT results, where the DFT+U-optimized cell parameters and estimated pressure values are employed. Fig. 2(a) shows projected densities of states (PDOS) of $NiPS_3$ with varying pressure from 0 to 88 GPa. It is clear that the t_{2g} states (a_g and e'_g) are mostly occupied, while the e_g states are partially filled and show a narrow dip at the Fermi level at 30.4 GPa. The self-energies of the e_g orbitals show poles at the Fermi level (see SI), confirming the presence of the paramagnetic Mott phase. Previously, it was suggested that $NiPS_3$ is a negative charge-transfer (NCT) insulator with a $d^9\underline{L}^1$ configuration ($\underline{L}$ denoting a S p-ligand hole) [29]. However, our eDMFT results show that when the Ni occupation is close to $n_d \approx 9$, where the $d^9\underline{L}^1$ configuration is dominant, the Mott insulating state cannot be stabilized, i.e., the material is metallic. The experimentally observed Mott insulating behavior can only be achieved with the Ni occupancy of $n_d \approx 8$, where the high-spin $S = 1$ configuration is dominant, i.e., corresponding to approximately half-filled e_g states (see Fig. 2(b) for the probability distribution in the insulating and metallic states). This observation is corroborated by X-ray absorption spectroscopy, indicating that $NiPS_3$ is close to the NCT regime, but is still dominated by the d^8 $S = 1$ configuration, consistent with our eDMFT results [30].

Fig. 2(b) shows the valence histogram for the few most important Ni d configurations versus pressure at $T = 232$K. The Mott insulating state is stable as long as the high-spin state ($|S_z| = 1$) of the Ni-d^8 configuration is dominant. Note that we report S_z values rather than S values, because of our choice of an Ising-type approximation of the Coulomb interaction in the eDMFT impurity solver [31]. Around 31 GPa the $|S_z| = 1/2$ states (of d^9 and d^7 configurations) become equally probable, at which point the Mott state collapses and a narrow metallic quasiparticle peak appears (see the third panel in Fig. 2(a)). Despite the enhanced charge fluctuation, the change of Ni d-orbital occupation (n_d) across the transition is negligible: n_d = 8.15 and 8.19 at P = 0 and 88 GPa, respectively. The increase of charge fluctuations with increasing pressure has an additional effect of unlocking the $|S_z| = 0$ sector of the d^8 configuration, which is favored in the itinerant low spin regime at large pressure. Note that the increase of the probability for $|S_z| = 0$ at the expense of the $|S_z| = 1$ state has a large effect on the size of the fluctuating moment $|2S_z|$, which is plotted

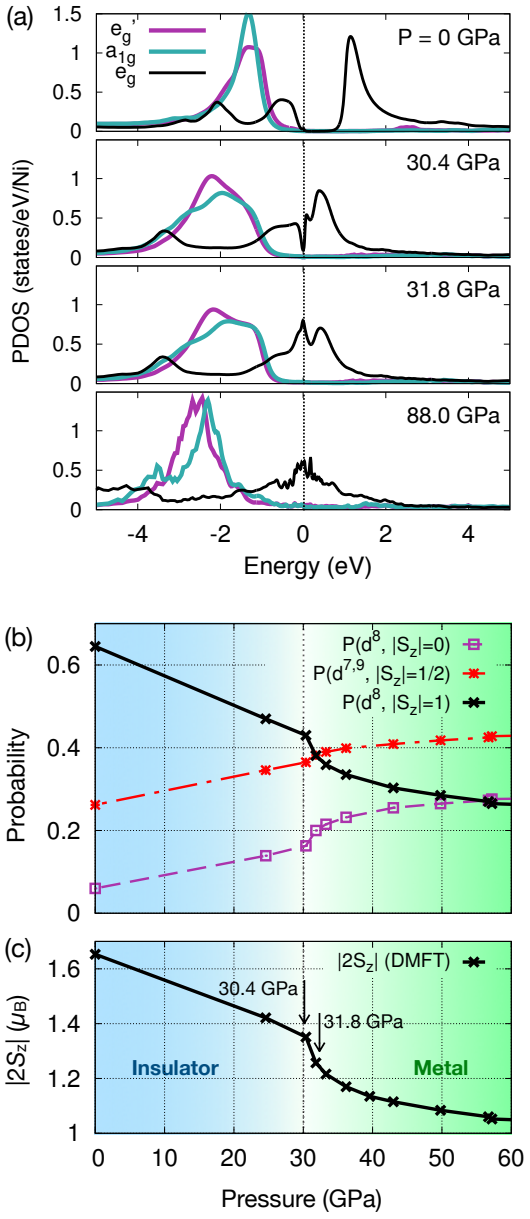

FIG. 2. (a) Projected density of states (PDOS) from paramagnetic (PM) eDMFT results ($T = 232$K) with the increasing pressure from the ambient condition (top panel) to 88 GPa (lowest). (b) Monte Carlo probabilities for the d^8 $|S_z| = 0$ (purple dashed line), $d^{7,9}$ $|S_z| = 1/2$ (red dash-dotted), and d^8 $|S_z| = 1$(black solid) as a function of pressure. (c) Pressure dependence of the size of PM Ni spin moment $|2S_z|$ from PM eDMFT results at $T = 232$K. Note a cusp at P = 30.4 GPa where the MIT happens.

in Fig. 2(c). Its zero-pressure value is around $1.6\,\mu_B$, which is quite reduced from the maximum atomic value of $2\,\mu_B$, and once it is reduced below $1.4\,\mu_B$ it drops very suddenly and takes values of $\leq 1.3\,\mu_B$ in the metallic state. We note that the change between 30.4 and 31.8 GPa is abrupt, which is likely associated with a first-order transition, for which a coexistence of both solutions is expected. However, we were not able to confirm the hysteresis, probably because it is too narrow at the

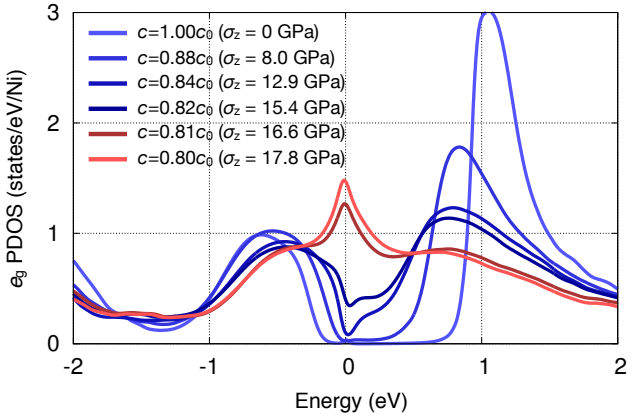

FIG. 3. $NiPSe_3$ e_g-PDOS in the presence of an uniaxial stress σ_z along the layer-normal $\hat{z}$-direction from PM eDMFT results (with varying σ_z from 0 to 17.8 GPa). Blue and red curves are PDOS for insulating and metallic phases, respectively, when the MIT happens between σ_z = 15.4 and 16.6 GPa.

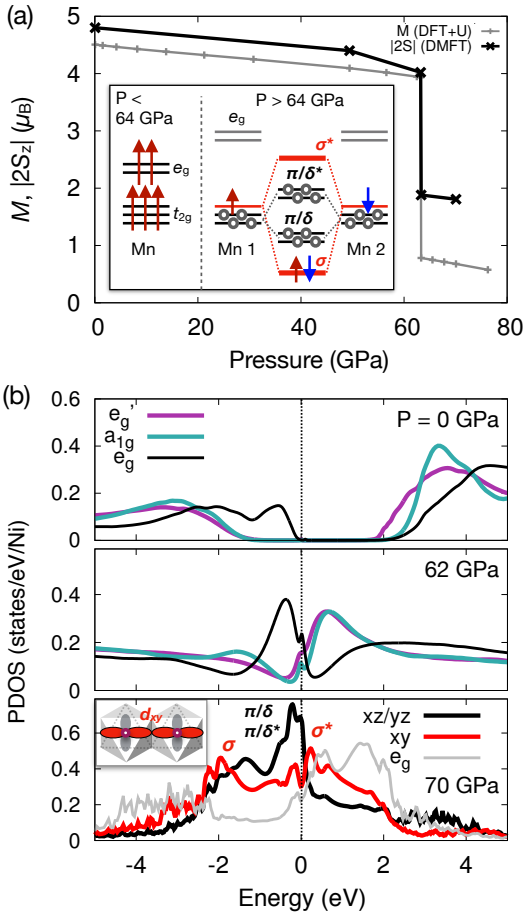

FIG. 4. (a) Pressure dependence of the size of Mn spin moment M from DFT+U (gray line) and $|2S_z|$ from paramagnetic eDMFT at T = 580K (black), where both results show the spin-state transition at 63 GPa. The schematic spin-orbital configurations below and above the transition are shown in the inset. (b) PDOS from eDMFT, at P = 0 GPa (upper panel), 62 GPa (center), and 70 GPa (lower). Note that the choice of d-orbital onto which the DOS are projected is different below and above the transition (e_g' and a_{1g} below, and $d_{xz,yz,xy}$ above 63 GPa).

temperature studied ($T = 232$ K).

MIT driven by uniaxial pressure in $NiPSe_3$. While the critical pressure for the MIT in $NiPS_3$ can be reached in modern high-pressure experimental setups, a substitution of S by the more polarizable Se is expected to further reduce the critical pressure. Therefore the recently synthesized $NiPSe_3$ [32] can be a better candidate for realizing the pressure-driven MIT compared to $NiPS_3$. Moreover, the collapse of the interlayer distance is expected to be sufficient to induce the MIT, which can even be achieved by the tip of an atomic-force microscope [33]. As a zeroth-order approximation, we simulate such layer-normal strain by varying the interlayer distance with fixed in-plane lattice parameters, and allowing the internal coordinates to relax within eDMFT. In Fig. 3 we show the e_g-PDOS of $NiPSe_3$ where the MIT happens at the modest stress of σ_z = 16 GPa. It is remarkable that such a large gap of 1 eV at the ambient pressure is collapsed by such a modest stress. No additional structural distortion is observed at the transition, which suggests that $NiPSe_3$ is another promising candidate for an electronic bandwidth-controlled Mott transition in these layered vdW materials.

Volume collapse and MIT in $MnPS_3$. We now address the volume-collapse transition in $MnPS_3$. We first checked that once the optimized lattice parameters from DFT+U are employed, both DFT+U and eDMFT optimizations for the internal coordinates yield practically the same result. Fig. 4(a) shows the evolution of the fluctuating Mn moment $|2S_z|$ within the PM eDMFT at T = 580 K. We also show the ordered magnetic moment M (per Mn) within DFT+U in the Néel-type antiferromagnetic ordered state [22, 26, 34] (grey line in the plot). Perhaps not surprisingly, the two methods show very similar behavior: an insulating state of almost maximum spin S = 5/2 configuration in the low-to-intermediate-P regime, and a metallic state with strongly reduced Mn moments above P = 64 GPa. The inset of Fig. 4(a) schematically depicts the spin-orbital configuration below and above the transition. In the presence of strong external pressure, the orbitally inert high-spin S = 5/2 configuration becomes energetically unstable, and the low-spin S = 1/2 with the partially filled t_{2g} orbital is stabilized with an octahedral volume collapse [35]. As a result, the t_{2g} open shell in this edge-sharing geometry leads to a strong σ-like direct d-d overlap between the nearest-neighboring (NN) Mn sites, resulting in a strong tendency toward Mn dimerization [36]. At ambient pressure, because of the weak inter-layer coupling, the three in-plane NN bonds are essentially equivalent to each other. In the high-pressure regime, however, the monoclinicity originating from the layer stacking is no longer negligible. Therefore, the NN bond parallel to the b direction, which becomes nonequivalent to the other bonds, dimerizes as shown in Fig. 1(d).

Discussion and Summary. Our findings suggest a relation between lattice structure and orbital degrees of freedom in

the edge-sharing octahedral geometry, which are commonly found in many vdW-layered chalcogenides and layered oxides. Specifically, in materials with edge-sharing octahedra, transition metal ions with an open t_{2g} shell will give rise to strong intermetallic covalency resulting in enhanced electron-lattice coupling and lattice distortions, as recently suggested [36] and experimentally observed [37, 38]. On the other hand, an open e_g shell, which can give rise to various interesting electronic and magnetic properties strongly coupled to the lattice in corner-shared perovskite systems [4, 5, 14, 39, 40], does not induce a strong electron-lattice coupling in these edge-shared geometries. Such insight can be utilized to devise enhanced structural, electronic and magnetic responses, thus providing a pathway to design principles for engineering functional correlated materials in these chalcogen-based compounds.

In summary, we report a first theoretical study of the Mott MIT induced by external pressure in strongly correlated layered vdW materials. The electronic bandwidth-controlled Mott transition in $NiPS_3$ and $NiPSe_3$ found in this study is especially deserving of further investigation for possible utilization in ultrafast resistivity switching in electronic and spintronic devices. The nature of Mott phases in other metal trisulfides, such as $FePS_3$ [23] or $CoPS_3$ [41], are also of great interest because of their partially filled t_{2g} shells even under ambient conditions. Overall, this family of vdW-layered transition metal trichalcogenides can be an excellent platform for the study of strong electron correlations and their cooperation with spin and lattice degrees of freedom.

Acknowledgments: We thank Janice L. Musfeldt and Sang-Wook Cheong for helpful discussions. The work was supported by NSF DMREF grant DMR-1629059.

[1] N. F. Mott and R. Peierls, Proceedings of the Physical Society **49**, 72 (1937).
[2] J. Hubbard, Proceedings of the Royal Society of London A: Mathematical, Physical and Engineering Sciences **276**, 238 (1963).
[3] J. G. Bednorz and K. A. Müller, Zeitschrift für Physik B Condensed Matter **64**, 189 (1986).
[4] J. B. Torrance, P. Lacorre, A. I. Nazzal, E. J. Ansaldo, and C. Niedermayer, Phys. Rev. B **45**, 8209 (1992).
[5] M. L. Medarde, Journal of Physics: Condensed Matter **9**, 1679 (1997).
[6] M. M. Qazilbash, K. S. Burch, D. Whisler, D. Shrekenhamer, B. G. Chae, H. T. Kim, and D. N. Basov, Phys. Rev. B **74**, 205118 (2006).
[7] F. J. Morin, Phys. Rev. Lett. **3**, 34 (1959).
[8] D. B. McWhan, J. P. Remeika, T. M. Rice, W. F. Brinkman, J. P. Maita, and A. Menth, Phys. Rev. Lett. **27**, 941 (1971).
[9] S. A. Carter, T. F. Rosenbaum, P. Metcalf, J. M. Honig, and J. Spalek, Phys. Rev. B **48**, 16841 (1993).
[10] M. M. Qazilbash, M. Brehm, B.-G. Chae, P.-C. Ho, G. O. Andreev, B.-J. Kim, S. J. Yun, A. V. Balatsky, M. B. Maple, F. Keilmann, H.-T. Kim, and D. N. Basov, Science **318**, 1750 (2007).
[11] K. Haule and G. L. Pascut, Scientific Reports **7**, 10375 (2017).
[12] S. Johnston, A. Mukherjee, I. Elfimov, M. Berciu, and G. A. Sawatzky, Phys. Rev. Lett. **112**, 106404 (2014).
[13] H. Park, A. J. Millis, and C. A. Marianetti, Phys. Rev. Lett. **109**, 156402 (2012).
[14] T. Mizokawa, D. I. Khomskii, and G. A. Sawatzky, Phys. Rev. B **61**, 11263 (2000).
[15] W. H. Brito, M. C. O. Aguiar, K. Haule, and G. Kotliar, Phys. Rev. Lett. **117**, 056402 (2016).
[16] S. Biermann, A. Poteryaev, A. I. Lichtenstein, and A. Georges, Phys. Rev. Lett. **94**, 026404 (2005).
[17] H.-T. Kim, Y. W. Lee, B.-J. Kim, B.-G. Chae, S. J. Yun, K.-Y. Kang, K.-J. Han, K.-J. Yee, and Y.-S. Lim, Phys. Rev. Lett. **97**, 266401 (2006).
[18] E. Arcangeletti, L. Baldassarre, D. Di Castro, S. Lupi, L. Malavasi, C. Marini, A. Perucchi, and P. Postorino, Phys. Rev. Lett. **98**, 196406 (2007).
[19] G. Stefanovich, A. Pergament, and D. Stefanovich, Journal of Physics: Condensed Matter **12**, 8837 (2000).
[20] D. Ruzmetov, G. Gopalakrishnan, C. Ko, V. Narayanamurti, and S. Ramanathan, Journal of Applied Physics **107**, 114516 (2010).
[21] Z. Yang, C. Ko, and S. Ramanathan, Annual Review of Materials Research **41**, 337 (2011).
[22] Y. Wang, Z. Zhou, T. Wen, Y. Zhou, N. Li, F. Han, Y. Xiao, P. Chow, J. Sun, M. Pravica, A. L. Cornelius, W. Yang, and Y. Zhao, J. Am. Chem. Soc. **138**, 15751 (2016).
[23] J.-G. Park, Journal of Physics: Condensed Matter **28**, 301001 (2016).
[24] K. Haule, Journal of the Physical Society of Japan **87**, 041005 (2018).
[25] For DFT+DMFT calculations we use the Rutgers DFT+Embedded DMFT code [42], while for DFT and DFT+U calculation we used the Vienna *Ab-initio* Simulation Package [43, 44]. For computational details refer to the Supplementary Information (SI).
[26] R. Brec, Solid State Ionics **22**, 3 (1986).
[27] A. R. Wildes, H. M. Rønnow, B. Roessli, M. J. Harris, and K. W. Godfrey, Phys. Rev. B **74**, 094422 (2006).
[28] A. R. Wildes, V. Simonet, E. Ressouche, G. J. McIntyre, M. Avdeev, E. Suard, S. A. J. Kimber, D. Lançon, G. Pepe, B. Moubaraki, and T. J. Hicks, Phys. Rev. B **92**, 224408 (2015).
[29] S. Y. Kim, T. Y. Kim, L. J. Sandilands, S. Sinn, M.-C. Lee, J. Son, S. Lee, K.-Y. Choi, W. Kim, B.-G. Park, C. Jeon, H.-D. Kim, C.-H. Park, J.-G. Park, S. J. Moon, and T. W. Noh, Phys. Rev. Lett. **120**, 136402 (2018).
[30] B. Pal, H.-S. Kim, K. Haule, D. Vanderbilt, J. Chakhalian, and J. Freeland, (2018), to be submitted.
[31] This approximation leads to some mixing between $S = 0$ and 1 states, but is not expected to change qualitative aspects of the results.
[32] J.-Q. Yan, B. C. Sales, M. A. Susner, and M. A. McGuire, Phys. Rev. Materials **1**, 023402 (2017).
[33] H. Lu, C.-W. Bark, D. Esque de los Ojos, J. Alcala, C. B. Eom, G. Catalan, and A. Gruverman, Science **336**, 59 (2012).
[34] K. Okuda, K. Kurosawa, S. Saito, M. Honda, Z. Yu, and M. Date, Journal of the Physical Society of Japan **55**, 4456 (1986).
[35] J. Kuneš, A. V. Lukoyanov, V. I. Anisimov, R. T. Scalettar, and W. E. Pickett, Nat. Mater. **7**, 198 EP (2008).
[36] S. V. Streltsov and D. I. Khomskii, Proc. Natl. Acad. Sci. U.S.A. **113**, 10491 (2016).
[37] L. S. I. Veiga, M. Etter, K. Glazyrin, F. Sun, C. A. Escanhoela, G. Fabbris, J. R. L. Mardegan, P. S. Malavi, Y. Deng, P. P.

Stavropoulos, H.-Y. Kee, W. G. Yang, M. van Veenendaal, J. S. Schilling, T. Takayama, H. Takagi, and D. Haskel, Phys. Rev. B **96**, 140402 (2017).
[38] V. Hermann, M. Altmeyer, J. Ebad-Allah, F. Freund, A. Jesche, A. A. Tsirlin, M. Hanfland, P. Gegenwart, I. I. Mazin, D. I. Khomskii, R. Valentí, and C. A. Kuntscher, Phys. Rev. B **97**, 020104 (2018).
[39] A. J. Millis, B. I. Shraiman, and R. Mueller, Phys. Rev. Lett. **77**, 175 (1996).
[40] A. J. Millis, Nature **392**, 147 EP (1998).
[41] A. R. Wildes, V. Simonet, E. Ressouche, R. Ballou, and G. J. McIntyre, Journal of Physics: Condensed Matter **29**, 455801 (2017).
[42] K. Haule, C.-H. Yee, and K. Kim, Phys. Rev. B **81**, 195107 (2010).
[43] G. Kresse and J. Hafner, Phys. Rev. B **47**, 558 (1993).
[44] G. Kresse and J. Furthmüller, Phys. Rev. B **54**, 11169 (1996).
[45] J. P. Perdew, A. Ruzsinszky, G. I. Csonka, O. A. Vydrov, G. E. Scuseria, L. A. Constantin, X. Zhou, and K. Burke, Phys. Rev. Lett. **100**, 136406 (2008).
[46] S. L. Dudarev, G. A. Botton, S. Y. Savrasov, C. J. Humphreys, and A. P. Sutton, Phys. Rev. B **57**, 1505 (1998).
[47] P. Blaha, K. Schwarz, G. K. H. Madsen, D. Kvasnicka, and J. Luitz, *WIEN2k, An Augmented Plane Wave + Local Orbitals Program for Calculating Crystal Properties* (Karlheinz Schwarz, Techn. Universität Wien, Austria, 2001).
[48] K. Haule and G. L. Pascut, Phys. Rev. B **94**, 195146 (2016).
[49] K. Haule and T. Birol, Phys. Rev. Lett. **115**, 256402 (2015).
[50] K. Haule, Phys. Rev. B **75**, 155113 (2007).
[51] A. A. Mostofi, J. R. Yates, G. Pizzi, Y.-S. Lee, I. Souza, D. Vanderbilt, and N. Marzari, Computer Physics Communications **185**, 2309 (2014).
[52] Q. Han, T. Birol, and K. Haule, Phys. Rev. Lett. **120**, 187203 (2018).
[53] J. Chen, A. J. Millis, and C. A. Marianetti, Phys. Rev. B **91**, 241111 (2015).

SUPPLEMENTARY INFORMATION: COMPUTATIONAL DETAILS

Density functional theory calculations

For unit cell optimizations and relaxations of initial internal coordinates, the Vienna *ab-initio* Simulation Package (VASP), which employs the projector-augmented wave (PAW) basis set [43, 44], was used for density functional theory (DFT) calculations in this work. 340 eV of plane-wave energy cutoff and 8×6×8 Monkhorst-Pack k-grid sampling were employed. For the treatment of electron correlations within DFT, a revised Perdew-Burke-Ernzerhof exchange-correlation functional for crystalline solid (PBEsol) was employed[45], in addition augmented by on-site Coulomb interactions for transition metal d-orbitals within a simplified rotationally-invariant form of DFT+$U_{\rm eff}$ formalism[46]. 10^{-4} eV/Å of force criterion was employed for structural optimizations.

Structural relaxations for all compounds were performed in the presence of the DFT+$U_{\rm eff}$ (4 eV) on-site Coulomb interaction and a Néel-type antiferromagnetic order[26], which gives reasonable agreements of lattice parameters and gap sizes with experimentally observed values[22, 29]. It should be mentioned that, without incorporating magnetism and $U_{\rm eff}$ to open the gap, the volume is severely underestimated for both compounds, especially $\sim$ 20% smaller in $MnPS_3$. This observation signifies the role of electron correlations in structural properties of these compounds.

Dynamical mean-field theory calculations

A fully charge-self-consistent dynamical mean-field method[42], implemented in Rutgers DFT + Embedded DMFT (eDMFT) Functional code (http://hauleweb.rutgers.edu/tutorials/) which is combined with WIEN2K code[47], is employed for computations of electronic properties and optimizations of internal coordinates[48]. In DFT level the Perdew-Wang local density approximation (LDA) is employed, which was argued to yield the best agreement of lattice properties combined with DMFT[49]. 500 k-points were used to sample the first Brillouin zone with $RK_{\rm max}$ = 7.0. A force criterion of 10^{-4} Ry/Bohr was adopted for optimizations of internal coordinates. A continuous-time quantum Monte Carlo method in the hybridization-expansion limit (CT-HYB) was used to solve the auxiliary quantum impurity problem[50], where the full 5 d-orbitals of Ni and Mn were chosen as our correlated subspaces in a single-site DMFT approximation. For the CT-HYB calculations, up to 10^{10} Monte Carlo steps were employed for each Monte Carlo run. In most runs temperature was set to be 232K, but in some calculations with high pressure it was increased up to 580K because of the increased hybridization between the impurity and bath. -10 to +10 eV of hybridization window (with respect to the Fermi level) was chosen, and U = 10 eV and $J_{\rm H}$ = 1 eV of on-site Coulomb interaction parameters were used for both Mn and Ni d-orbitals. Because of the large hybridization window, DMFT needs larger values of U to reproduce a reasonable agreement with experimental results compared to DFT+U, and shows weak material dependence of U and $J_{\rm H}$ values. A simplified Ising-type (density-density terms only) Coulomb interactions was employed in this work, and it was tested that the use of full Coulomb interaction yields only quantitatively different results in terms of pressure-induced evolution of electronic structures. A nominal double counting scheme was used, with the d-orbital occupations for double counting corrections for Ni and Mn were chosen to be 8 and 5, respectively.

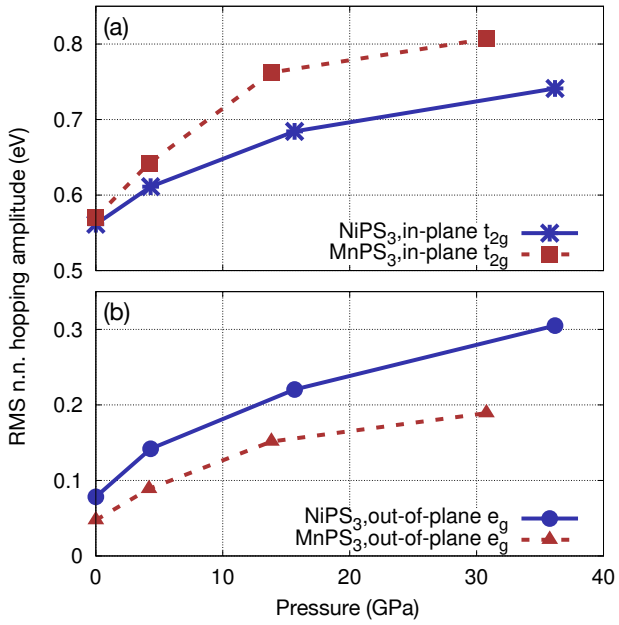

FIG. S5. Root mean square (RMS) of nearest-neighbor (n.n.) Wannier hopping amplitudes for Ni and Mn d-orbitals as a function of pressure, where the RMS of (a) in-plane t_{2g}-t_{2g} and (b) out-of-plane e_g-e_g are shown.

IN-PLANE AND OUT-OF-PLANE HOPPING AMPLITUDES

Fig. S5(a) and (b) show root mean square (RMS) amplitudes of nearest-neighbor (n.n.) in-plane t_{2g} and out-of-plane e_g hopping integrals, respectively, for $MnPS_3$ and $NiPS_3$. The d-orbital hopping integrals were computed using WANNIER90 package[51], employing optimized crystal structures in the presence of external pressure, without including $U_{\rm eff}$ and magnetism.

As shown in Fig. 1(a) and (b) in the main text, the in-plane lattice parameters (with respect to their ambient pressure value) a/a_0 and b/b_0 for $MnPS_3$ around 30 GPa are smaller by $\sim$ 2% compared to those of $NiPS_3$, while the out-of-plane c/c_0 of $MnPS_3$ is larger than that of $NiPS_3$. In accordance with the tendency of lattice parameter changes, the

enhancement of RMS in-plane t_{2g} hopping integrals is more pronounced in $MnPS_3$, which drives the formation of in-plane Mn dimer formation after the transition to the low-spin state with the open t_{2g} shell. Note that, the in-plane t_{2g} hopping integrals for Ni is also enhanced as the pressure is increased, but its effect is not significant due to the closed t_{2g} shell in the Ni d^8 configuration. Similarly, the enhanced out-of-plane kinetic energy between the e_g orbitals in $NiPS_3$, depicted in Fig. S5(b), induces more pronounced reduction of the c parameter in $NiPS_3$ compared to that of $MnPS_3$. It should be mentioned that, while the out-of-plane e_g hopping terms are also enhanced in $MnPS_3$, their role in structural response to pressure is less significant both in the low- and high-pressure regimes; in the low-pressure regime the hybridization between the d^5 high-spin Mn ion and anions is weak, and so is the electron-lattice coupling, while in the high-pressure regime the high-spin Mn has empty e_g shell.

ELECTRONIC STRUCTURES WITH A NÉEL ORDER

Ambient pressure cases for both compounds

Fig. S6 shows the spectral functions of $NiPS_3$ (a-c) and $MnPS_3$ (d-f) with a Néel-type antiferromagnetic (AF) order in comparison with the paramagnetic (PM) phases. In both compounds, the presence of magnetism does not alter the size of charge gap, consistent with the Mott character of the insulating phases in both compounds. As the temperature is lowered and magnetism sets in, the broadening of spectral functions due to the imaginary part of self-energy is weakened. Indeed, DFT+U PDOS with the magnetic order shows very similar qualitative features with DMFT PDOS at T=58K (not shown).

Note that, the use of the Ising-type Coulomb repulsion gives rise to the stabilization of magnetic order well above the Néel temperatures of both compounds, T_N = 154 and 78 K for $NiPS_3$ and $MnPS_3$, respectively[26–28], as reported in previous DFT+DMFT studies[52]. It is argued that a larger in-plane kinetic energy scale originating from the e_g orbital in Ni yields the higher T_N in $NiPS_3$ compared to $MnPS_3$[29]. Despite the overestimated T_N, such tendency can be noticed in our results by comparing Fig. S6(b) and (e). While the size of the Ni magnetization in $NiPS_3$ ($2S_{\rm Ni}$ = 1.45 $\mu_{\rm B}$) is almost saturated to the value of PM moment ($|2S_{\rm Ni}|$ = 1.65 $\mu_{\rm B}$), even at T = 232K, the Mn magnetization in $MnPS_3$ at the same T is $2S_{\rm Mn}$ = 0.87 $\mu_{\rm B}$, just a fraction of the S = 5/2 moment size (4.80 $\mu_{\rm B}$) of the high-spin Mn. As T is lowered to 58K, magnetizations in both compounds saturate to the local moment size, as shown in Fig. S6(c) and (f).

Near the MIT critical pressure

$MnPS_3$

As discussed in the main text, the pressure-induced MIT in $MnPS_3$ in the paramagnetic phase is a discontinuous transition accompanied by a spin-state transition and isosymmetric structural distortion with a volume collapse. Such discontinuous character does not change in the presence of magnetism, as shown in Fig. S8, where the change of the Mn magnetization M (per Mn) from DFT+U and eDMFT results (at T = 232 K) are shown as a function of pressure. Note that, the upturn of M in the small-pressure regime ($<$ 10 GPa) in eDMFT is due to the enhancement of magnetic exchange interactions originating from increased kinetic energy scale under the pressure.

$NiPS_3$

In the PM phase of $NiPS_3$, the MIT can be indicated not only by the gap opening in the PDOS, but also by the change of electron self-energies $\Sigma(\omega)$. In Fig. S7(a) and (c), the MIT can be noticed by the presence and absence of the dip at the Fermi level in their PDOS, but it is slightly unclear whether the phase at P = 30.4 GPa is an insulator due to the small but finite e_g DOS at the Fermi level due to the broadening. However, $\Im\Sigma(\omega)$, plotted in Fig. S7(b) and (d), show a clear difference between the two phases, because the presence (absence) of a pole at the Fermi level in the e_g-$\Im\Sigma(\omega)$ signifies the presence (absence) of the Mott physics.

In the AF-ordered phases, the gap opening is induced by the exchange splitting between the spin up and down components, *i.e.* $\Re\left(\Sigma_{\rm up}-\Sigma_{\rm down}\right)(\omega)$. In cases where $\Im\Sigma(\omega)$ is weak compared to $\Re\Sigma(\omega)$ and the frequency dependence of $\Re\left(\Sigma_{\rm up}-\Sigma_{\rm down}\right)(\omega)$ is small, then the eDMFT results become equivalent to the DFT+U results. Fig. S7(e-j) present such situation, where the PDOSs shown in Fig. S7(e) and (h) become qualitatively equivalent to DFT+U PDOS (not shown), with the exchange splitting of $\sim$ 4 eV at the Fermi level opening a gap for the e_g bands. Hence, in AF phases the MIT critical pressure is mainly determined by the e_g bandwidth and the exchange splitting $\Re\left(\Sigma_{\rm up}-\Sigma_{\rm down}\right)(\omega)$. Because the above quantities change continuously as the pressure is increased, it is not easy to point out at which pressure the MIT happens from the PDOS plots due to the presence of small broadening from $\Im\Sigma(\omega)$. At T = 232K, the MIT seems to happen around 24 GPa, and this pressure does not change as T is lowered to 116K.

Fig. S9(a) depicts the change of Ni magnetizations from DFT+U and AF-eDMFT as a function of pressure. Note that, the MIT critical pressures are 36 and 24 $\sim$ 30 GPa for DFT+U and AF-eDMFT results, as shown in the figure, but the magnetization persists within the metallic phase. The pressure where the magnetism disappears in AF-eDMFT results increases slightly from 36 to 40 GPa as the T is reduced from

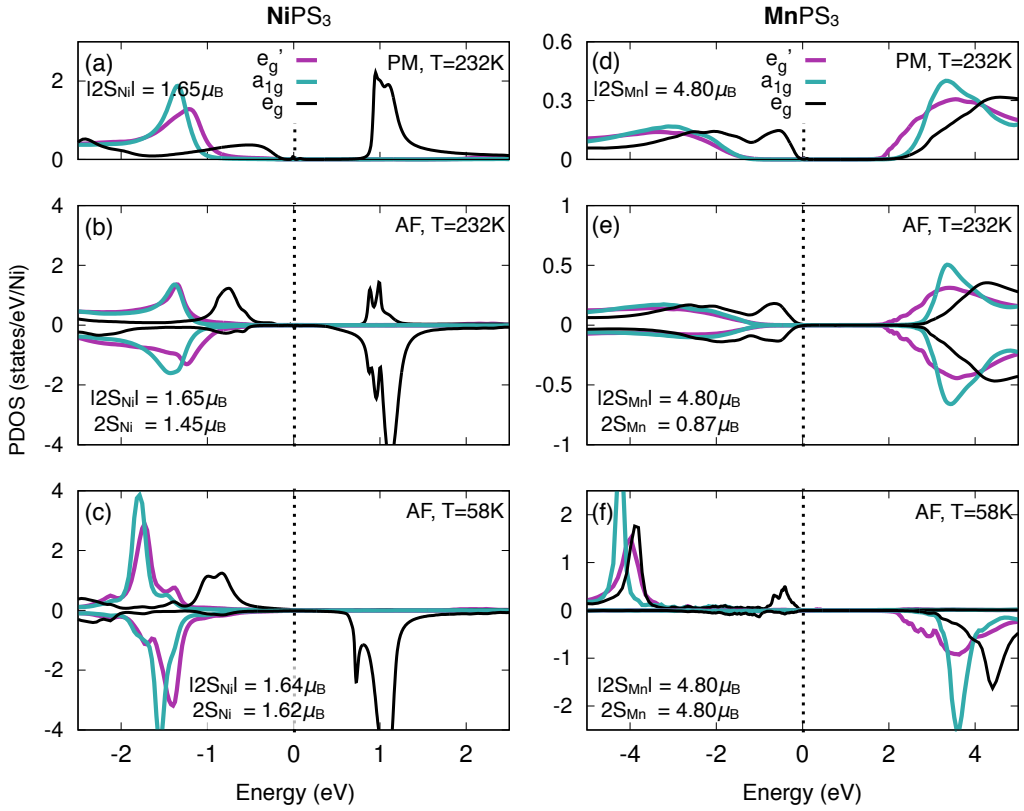

FIG. S6. (a-c) PDOS of $NiPS_3$ and (d-f) $MnPS_3$ with a Néel type antiferromagnetic (AF) order (b,c,e,f) in comparison with paramagnetic (PM) PDOS (a,d). The second and third rows show AF PDOS with T = 232K and 58K, respectively.

232K to 116K, but it does not reach 58 GPa where the magnetization disappears in DFT+U results. Note that, the high-pressure anisotropic structural distortion in $NiPS_3$ happens at the pressure where the DFT+U magnetization becomes zero.

Fig. S9(b) shows the change of Ni local spin moment size $|2S|$ as a function of pressure. Unlike the $|2S|$ in the PM phase, which shows a cusp at the MIT critical pressure, $|2S|$ in the AF phases does not show such behavior at the MIT pressure. As the pressure is increased, the AF $|2S|$ is suppressed until the magnetization disappears and a PM metallic phase happens. Note that, the pressures that AF $|2S|$ joins the PM $|2S|$ curve are the points where the magnetization disappears.

COMPARISON WITH DFT+U AND DMFT IN $MnPS_3$

As marked in Fig. 1(a) in the main text, the value of critical pressure predicted by DFT+U calculations is twice bigger than the one reported in Ref. 22 (63 vs. 30 GPa). For a better understanding of this discrepancy, we perform calculations with interpolating structures between the honeycomb high-spin and the dimerized low-spin structures as shown in Fig. S10. Because the computation of stress tensor is not yet available in the current eDMFT formalism, two constant-volume cuts at V = 0.57 and 0.54 V_0 are taken for a total energy comparison as shown in Fig. S10(a). For DFT+U results, high-spin and low-spin states are first converged in their honeycomb and dimerized structures respectively, and then the crystal structures are slowly distorted towards the other side while maintaining the local minima spin states.

Fig. S10(b) and (c) are relative total energies and size of spin moments from the high-, low-spin DFT+U, and paramagnetic eDMFT calculations at V = 0.57 V_0. A remarkable feature is, while the energy difference between the high- and low-spin ground states is 1.72 eV in DFT+U, it is 0.58 eV in eDMFT, which is almost one third of the DFT+U value. Furthermore, while the high- and low-spin local minima states remain (meta)stable even after the structural changes, as shown in Fig. S10(c), in eDMFT we have a spin-state crossover as the structure evolve from one limit to another. This features persist at V = 0.54 V_0 (Fig. S10(d,e)), where the height of the energy barrier from the high-spin to the low-spin state (0.3 eV) is substantially suppressed (60 meV) with the same spin-state crossover. These observations show that, the dynamical fluctuation effect inherent in eDMFT causes mixing between different spin configurations, hence introducing the crossover behavior shown in Fig. S10(c) and (e) and suppressing the energy differences. This observation is consistent with a previous DFT+DMFT study on a spin-state-crossover molecule[53]. Note that, our analysis here does not explicitly predict that the low-spin state is stabilized at lower pressure in eDMFT results shown in Fig. 1(a) in the main text. However,

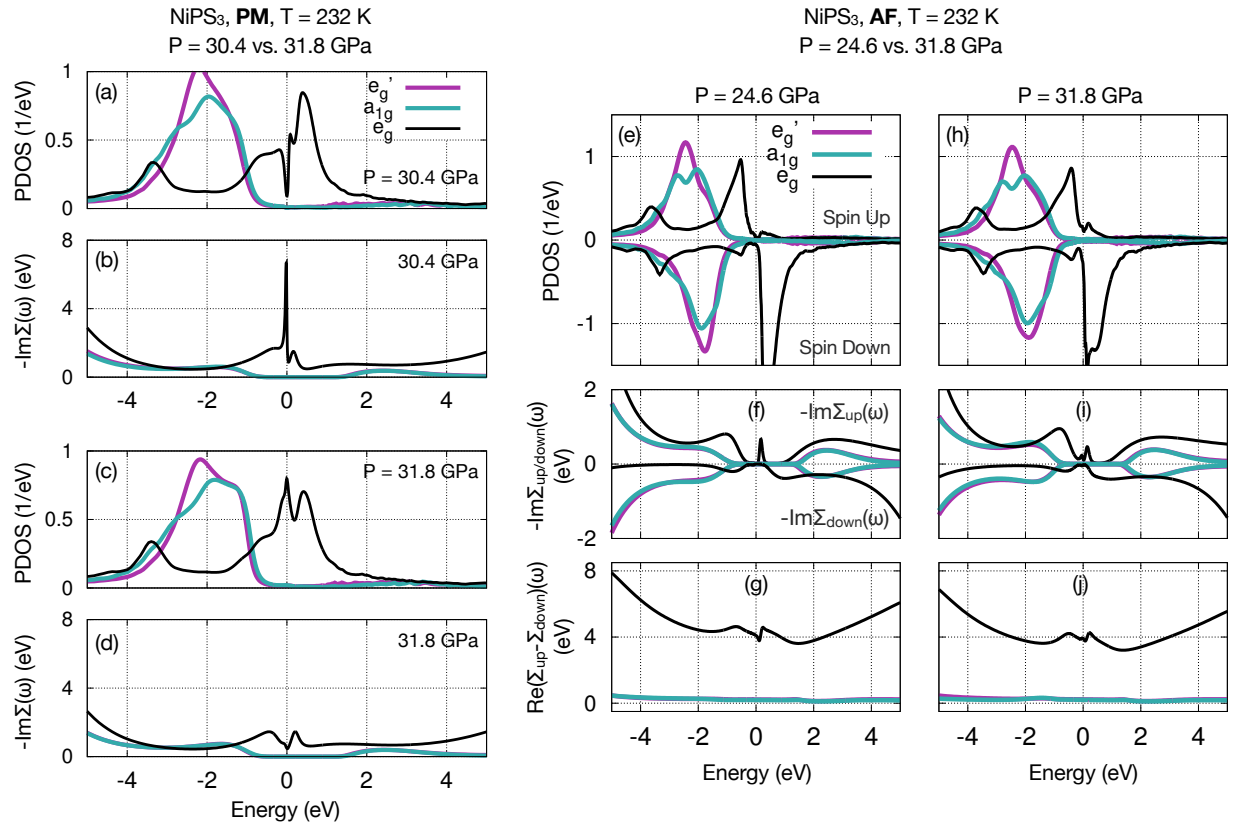

FIG. S7. PDOS and electron self-energies $\Sigma(\omega)$ of (a-d) PM and (e-j) AF $NiPS_3$ at $T = 232$K. The imaginary part of PM self-energies in (b) and (d) show a clear e_g peak and its absence in the Mott-insulating and metallic phases, respectively. (e) and (h) show spin- and orbital-projected PDOS at P = 24.6 and 31.8 GPa, respectively (spin up and down PDOS plotted in positive and negative values respectively). Imaginary part of $\Sigma(\omega)$, plotted in (f) and (i), show the absence of peak near the Fermi level. (e) and (h) show the difference between the real part of spin up and down self-energies $\Re\left(\Sigma_{\rm up} - \Sigma_{\rm down}\right)(\omega)$, which is the on-site exchange splitting opening the gap in the magnetic phases. Note that, the MIT point is not clear due to the smearing of spin up and down e_g bands in the PDOS.

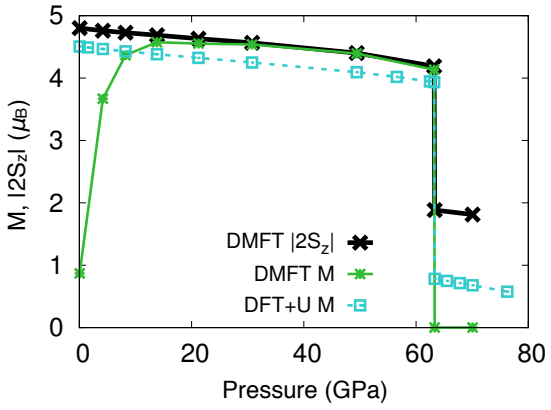

FIG. S8. Evolution of sizes of DFT+U and eDMFT local moments $|2S_z|$ and Mn magnetization M (per Mn) in $MnPS_3$ as a function of pressure. eDMFT results are obtained at T = 232 K with the Néel order.

since the energy difference between different states is reduced to a fraction compared to DFT+U results, the value of critical pressure should be reduced after the lattice free energy contribution and the zero-point fluctuation ignored in this work are included.

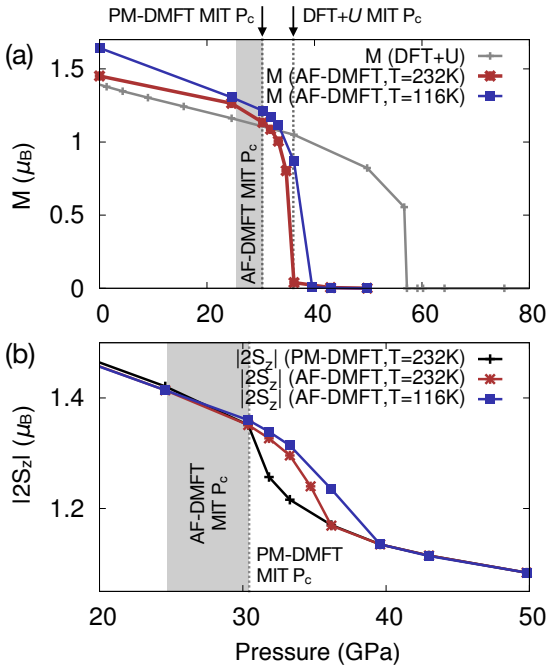

FIG. S9. (a) Evolution of Ni magnetization M (per Ni) from DFT+U (gray curve), AF-eDMFT at T = 232 (red) and 58K (blue) as a function of pressure. The MIT critical pressures from DFT+U, PM- and AF-eDMFT are depicted. (b) Sizes of Ni spin moments $|2S|$ from PM- and AF-eDMFT results.

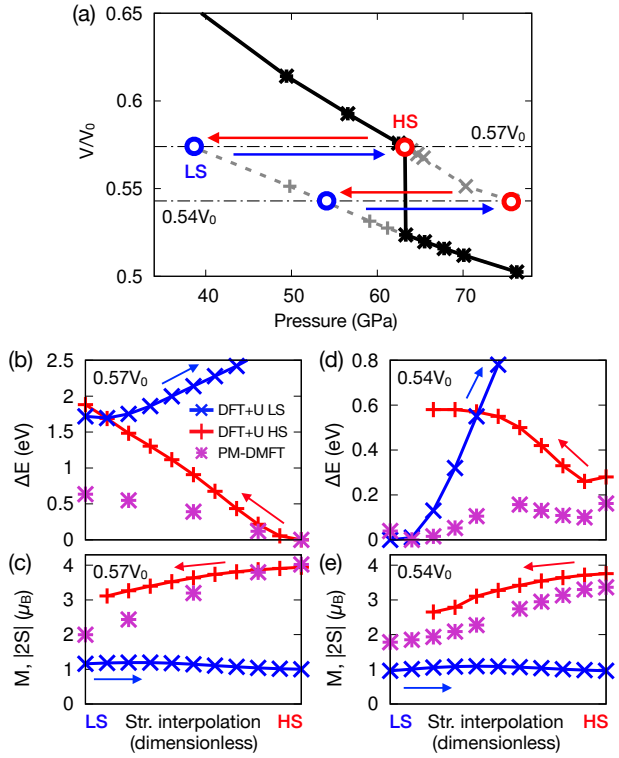

FIG. S10. (a) A magnified view of the $MnPS_3$ volume vs. pressure plot, where the black solid and gray dashed lines are curves for ground and metastable states respectively. Two dash-dotted lines are at V = 0.57 and 0.54 V_0 on which structural interpolations between the high-spin honeycomb and low-spin dimerized structures are made. (b,c) Total energy differences (b) and size of Mn moments (c) as a function of structural interpolation at V = 0.57 V_0, where red (blue) curve depicting total energy and Mn magnetization starting from high-spin (low-spin) structure and approaching to the low-spin (high-spin) side, and purple symbols depicting same results from paramagnetic eDMFT calculations at T = 580K. (d,e) Same plots at V = 0.54 V_0. Size of QMC error bars for eDMFT results are 4 meV at most, smaller then the symbol size.